Astroparticle Physics 34 (2010) 48–58

Contents lists available at ScienceDirect

Astroparticle Physics

journal homepage: www.elsevier.com/locate/astropart

The energy spectrum of atmospheric neutrinos between 2 and 200 TeV with the AMANDA-II detector

R. Abbasi [ab], Y. Abdou [v], T. Abu-Zayyad [ag], J. Adams [p], J.A. Aguilar [ab], M. Ahlers [af], K. Andeen [ab], J. Auffenberg [am], X. Bai [ae], M. Baker [ab], S.W. Barwick [x], R. Bay [g], J.L. Bazo Alba [an], K. Beattie [h], J.J. Beatty [r,s], S. Bechet [m], J.K. Becker [j,*], K.-H. Becker [am], M.L. Benabderrahmane [an], J. Berdermann [an], P. Berghaus [ab], D. Berley [q], E. Bernardini [an], D. Bertrand [m], D.Z. Besson [z], M. Bissok [a], E. Blaufuss [q], D.J. Boersma [a], C. Bohm [ah], S. Böser [k], O. Botner [ak], L. Bradley [aj], J. Braun [ab], S. Buitink [h], M. Carson [v], D. Chirkin [ab], B. Christy [q], J. Clem [ae], F. Clevermann [t], S. Cohen [y], C. Colnard [w], D.F. Cowen [aj,ai], M.V. D'Agostino [g], M. Danninger [ah], C. De Clercq [n], L. Demirörs [y], O. Depaepe [n], F. Descamps [v], P. Desiati [ab], G. de Vries-Uiterweerd [v], T. DeYoung [aj], J.C. Díaz-Vélez [ab], J. Dreyer [j], J.P. Dumm [ab], M.R. Duvoort [al], R. Ehrlich [q], J. Eisch [ab], R.W. Ellsworth [q], O. Engdegård [ak], S. Euler [a], P.A. Evenson [ae], O. Fadiran [d], A.R. Fazely [f], A. Fedynitch [j], T. Feusels [v], K. Filimonov [g], C. Finley [ah], M.M. Foerster [aj], B.D. Fox [aj], A. Franckowiak [i], R. Franke [an], T.K. Gaisser [ae], J. Gallagher [aa], R. Ganugapati [ab], M. Geisler [a], L. Gerhardt [h,g], L. Gladstone [ab], T. Glüsenkamp [a], A. Goldschmidt [h], J.A. Goodman [q], D. Grant [u], T. Griesel [ac], A. Groß [p,w], S. Grullon [ab], R.M. Gunasingha [f], M. Gurtner [am], C. Ha [aj], A. Hallgren [ak], F. Halzen [ab], K. Han [p], K. Hanson [ab], K. Helbing [am], P. Herquet [ad], S. Hickford [p], G.C. Hill [ab], K.D. Hoffman [q], A. Homeier [i], K. Hoshina [ab], D. Hubert [n], W. Huelsnitz [q], J.-P. Hülß [a], P.O. Hulth [ah], K. Hultqvist [ah], S. Hussain [ae], R.L. Imlay [f], A. Ishihara [o], J. Jacobsen [ab], G.S. Japaridze [d], H. Johansson [ah], J.M. Joseph [h], K.-H. Kampert [am], A. Kappes [ab,1], T. Karg [am], A. Karle [ab], J.L. Kelley [ab], N. Kemming [i], P. Kenny [z], J. Kiryluk [h,g], F. Kislat [an], S.R. Klein [h,g], S. Knops [a], J.-H. Köhne [t], G. Kohnen [ad], H. Kolanoski [i], L. Köpke [ac], D.J. Koskinen [aj], M. Kowalski [k], T. Kowarik [ac], M. Krasberg [ab], T. Krings [a], G. Kroll [ac], K. Kuehn [r], T. Kuwabara [ae], M. Labare [m], S. Lafebre [aj], K. Laihem [a], H. Landsman [ab], R. Lauer [an], R. Lehmann [i], D. Lennarz [a], J. Lünemann [ac], J. Madsen [ag], P. Majumdar [an], R. Maruyama [ab], K. Mase [o], H.S. Matis [h], M. Matusik [am], K. Meagher [q], M. Merck [ab], P. Mészáros [ai,aj], T. Meures [a], E. Middell [an], N. Milke [t], T. Montaruli [ab,2], R. Morse [ab], S.M. Movit [ai], K. Münich [t,**], R. Nahnhauer [an], J.W. Nam [x], U. Naumann [am], P. Nießen [ae], D.R. Nygren [h], S. Odrowski [w], A. Olivas [q], M. Olivo [ak,j], M. Ono [o], S. Panknin [i], L. Paul [a], C. Pérez de los Heros [ak], J. Petrovic [m], A. Piegsa [ac], D. Pieloth [t], R. Porrata [g], J. Posselt [am], P.B. Price [g], M. Prikockis [aj], G.T. Przybylski [h], K. Rawlins [c], P. Redl [q], E. Resconi [w], W. Rhode [t,***], M. Ribordy [y], A. Rizzo [n], J.P. Rodrigues [ab], P. Roth [q], F. Rothmaier [ac], C. Rott [r], C. Roucelle [w], T. Ruhe [t], D. Rutledge [aj], B. Ruzybayev [ae], D. Ryckbosch [v], H.-G. Sander [ac], S. Sarkar [af], K. Schatto [ac], S. Schlenstedt [an], T. Schmidt [q], D. Schneider [ab], A. Schukraft [a], A. Schultes [am], O. Schulz [w], M. Schunck [a], D. Seckel [ae], B. Semburg [am], S.H. Seo [ah], Y. Sestayo [w], S. Seunarine [l], A. Silvestri [x], A. Slipak [aj], G.M. Spiczak [ag], C. Spiering [an], M. Stamatikos [r,3], T. Stanev [ae], G. Stephens [aj], T. Stezelberger [h], R.G. Stokstad [h], S. Stoyanov [ae], E.A. Strahler [n], T. Straszheim [q], G.W. Sullivan [q], Q. Swillens [m], I. Taboada [e], A. Tamburro [ag], O. Tarasova [an], A. Tepe [e], S. Ter-Antonyan [f], S. Tilav [ae], P.A. Toale [aj], D. Tosi [an], D. Turčan [q], N. van Eijndhoven [n], J. Vandenbroucke [g], A. Van Overloop [v], J. van Santen [i], B. Voigt [an], C. Walck [ah], T. Waldenmaier [i], M. Wallraff [a], M. Walter [an], C. Wendt [ab], S. Westerhoff [ab], N. Whitehorn [ab], K. Wiebe [ac], C.H. Wiebusch [a], G. Wikström [ah], D.R. Williams [b], R. Wischnewski [an], H. Wissing [q], K. Woschnagg [g], C. Xu [ae], X.W. Xu [f], G. Yodh [x], S. Yoshida [o], P. Zarzhitsky [b]

[a] III. Physikalisches Institut, RWTH Aachen University, D-52056 Aachen, Germany
[b] Department of Physics and Astronomy, University of Alabama, Tuscaloosa, AL 35487, USA
[c] Department of Physics and Astronomy, University of Alaska Anchorage, 3211 Providence Dr., Anchorage, AK 99508, USA
[d] CTSPS, Clark-Atlanta University, Atlanta, GA 30314, USA
[e] School of Physics and Center for Relativistic Astrophysics, Georgia Institute of Technology, Atlanta, GA 30332, USA
[f] Department of Physics, Southern University, Baton Rouge, LA 70813, USA

0927-6505/$ - see front matter
doi:10.1016/j.astropartphys.2010.05.001

[g] Department of Physics, University of California, Berkeley, CA 94720, USA
[h] Lawrence Berkeley National Laboratory, Berkeley, CA 94720, USA
[i] Institut für Physik, Humboldt-Universität zu Berlin, D-12489 Berlin, Germany
[j] Fakultät für Physik & Astronomie, Ruhr-Universität Bochum, D-44780 Bochum, Germany
[k] Physikalisches Institut, Universität Bonn, Nussallee 12, D-53115 Bonn, Germany
[l] Department of Physics, University of the West Indies, Cave Hill Campus, Bridgetown BB11000, Barbados
[m] Université Libre de Bruxelles, Science Faculty CP230, B-1050 Brussels, Belgium
[n] Vrije Universiteit Brussel, Dienst ELEM, B-1050 Brussels, Belgium
[o] Department of Physics, Chiba University, Chiba 263-8522, Japan
[p] Department of Physics and Astronomy, University of Canterbury, Private Bag 4800, Christchurch, New Zealand
[q] Department of Physics, University of Maryland, College Park, MD 20742, USA
[r] Department of Physics and Center for Cosmology and Astro-Particle Physics, Ohio State University, Columbus, OH 43210, USA
[s] Department of Astronomy, Ohio State University, Columbus, OH 43210, USA
[t] Department of Physics, TU Dortmund University, D-44221 Dortmund, Germany
[u] Department of Physics, University of Alberta, Edmonton, Alberta, Canada T6G 2G7
[v] Department of Subatomic and Radiation Physics, University of Gent, B-9000 Gent, Belgium
[w] Max-Planck-Institut für Kernphysik, D-69177 Heidelberg, Germany
[x] Department of Physics and Astronomy, University of California, Irvine, CA 92697, USA
[y] Laboratory for High Energy Physics, École Polytechnique Fédérale, CH-1015 Lausanne, Switzerland
[z] Department of Physics and Astronomy, University of Kansas, Lawrence, KS 66045, USA
[aa] Department of Astronomy, University of Wisconsin, Madison, WI 53706, USA
[ab] Department of Physics, University of Wisconsin, Madison, WI 53706, USA
[ac] Institute of Physics, University of Mainz, Staudinger Weg 7, D-55099 Mainz, Germany
[ad] Université de Mons, 7000 Mons, Belgium
[ae] Bartol Research Institute and Department of Physics and Astronomy, University of Delaware, Newark, DE 19716, USA
[af] Department of Physics, University of Oxford, 1 Keble Road, Oxford OX1 3NP, UK
[ag] Department of Physics, University of Wisconsin, River Falls, WI 54022, USA
[ah] Oskar Klein Centre and Department of Physics, Stockholm University, SE-10691 Stockholm, Sweden
[ai] Department of Astronomy and Astrophysics, Pennsylvania State University, University Park, PA 16802, USA
[aj] Department of Physics, Pennsylvania State University, University Park, PA 16802, USA
[ak] Department of Physics and Astronomy, Uppsala University, Box 516, S-75120 Uppsala, Sweden
[al] Department of Physics and Astronomy, Utrecht University/SRON, NL-3584 CC Utrecht, The Netherlands
[am] Department of Physics, University of Wuppertal, D-42119 Wuppertal, Germany
[an] DESY, D-15735 Zeuthen, Germany

ARTICLE INFO

Article history:
Received 14 April 2010
Received in revised form 11 May 2010
Accepted 13 May 2010
Available online 20 May 2010

Keywords:
Atmospheric neutrinos
Unfolding
Neural net
AMANDA
Cherenkov radiation

ABSTRACT

The muon and anti-muon neutrino energy spectrum is determined from 2000–2003 AMANDA telescope data using regularised unfolding. This is the first measurement of atmospheric neutrinos in the energy range 2–200 TeV. The result is compared to different atmospheric neutrino models and it is compatible with the atmospheric neutrinos from pion and kaon decays. No significant contribution from charm hadron decays or extraterrestrial neutrinos is detected. The capabilities to improve the measurement of the neutrino spectrum with the successor experiment IceCube are discussed.

1. Introduction

At energies above 0.1 TeV, about one cosmic ray particle per square meter per second reaches Earth. At the highest-observed energies, particles reach more than 10^{20} eV, which is far above what can be achieved in man-made accelerators. The origin of these charged cosmic rays is still being discussed, as their direction is scrambled by extragalactic and galactic magnetic fields. One option for identifying the origin of cosmic rays is the observation of secondary particles produced in cosmic ray interactions in the astrophysical plasmas themselves: if a proton p interacts with ambient matter or photon fields γ, pionic secondaries are produced via the processes $p + p \to \pi + X$ and $p + \gamma \to \Delta^+ \to n + \pi^+/p + \pi^0$, respectively [4]. The charged pions subsequently decay into neutrinos, $\pi^\pm \to \mu^\pm + \nu_\mu \to e^\pm + \nu_e + \nu_\mu + \nu_\mu$, where we do not distinguish between neutrinos and anti-neutrinos. The resulting neutrino flux usually follows the spectral behaviour of the protons, which is predicted to be close to $dN/dE \propto E^{-2}$ according to Fermi acceleration (Fermi [18,19]). The conventional atmospheric neutrino spectrum due to pion and kaon decay, on the other hand, shows a spectral behaviour of approximately $dN/dE \propto E^{-3.7}$ [30,41,21,5,31]. An additional component of the atmospheric neutrino flux comes from the decays of hadrons containing charm and bottom quarks. This flux, known as the prompt component is expected to have a spectrum close to $dN/dE \propto E^{-2.7}$ [e.g. 11,14,20,35,31]. The prompt atmospheric neutrino flux is lower than the conventional flux but could start to dominate the total spectrum at energies above about 100 TeV. So far, only the conventional neutrino flux is observed [2]. Measurements at high-energies, i.e. above 10–100 TeV, provide an opportunity to reveal an extraterrestrial or a charm component. At these energies, the Antarctic Muon And Neutrino Detector Array (AMANDA) and its successor IceCube are able to make measurements to look for deviations from the conventional atmospheric neutrino flux.

* Corresponding author. Tel.: +49 234 3223779.
** Corresponding author.
*** Corresponding author.
E-mail address: julia.becker@rub.de (J.K. Becker).
[1] Universität Erlangen-Nürnberg, Physikalisches Institut, D-91058, Erlangen, Germany.
[2] Also at: INFN-Sezione di Bari, Italy.
[3] NASA Goddard Space Flight Center, Greenbelt, MD 20771, USA.

The AMANDA-II detector was designed for the detection of neutrinos above 100 GeV. It is composed of 677 Optical Modules (OMs), each containing a 8-inch, 14-dynode Photomultiplier Tube (PMT) and a voltage divider for the high-voltage. The PMTs are optically coupled to the pressure glass sphere with a silicon gel and can be operated at a high-gain of about $1 \cdot 10^9$. The optical modules are attached to 19 vertical strings, instrumenting a cylindrical volume of 0.016 km^3 (with a radius of 100 m and a height of 500 m), see e.g. DeYoung et al. [16]. Secondary muons in the ice are produced via the process $\nu_\mu + N \rightarrow \mu + X$.[4] The muons produce Cherenkov radiation if they travel faster than the speed of light in ice (i.e. if the muons travel faster than $v > 0.8 \cdot c_0$, with c_0 as the speed of light in vacuum). Additional Cherenkov radiation comes from the particles produced in muon interactions, such as bremsstrahlung, direct pair production and photonuclear interactions, all dominating at muon energies above 1 TeV. At higher-energies, the sum of the energy loss due to stochastic processes (i.e. bremsstrahlung, pair production and nuclear interaction) is dominant and increases linearly with the energy. The amount of light detected with the optical modules rises with the muon energy and therefore also with the energy of the parent neutrino. Thus the detected light amount can be used to determine the primary neutrino energy spectrum. Neutrino-induced muons can be distinguished from atmospheric muons by selecting events that traverse the Earth and arrive at the detector from below the horizon. Atmospheric muons cannot reach the detector from those directions since they are absorbed on their way through the Earth. In this energy range ($E < 200$ TeV), neutrino absorption in the Earth is not significant. Neutrinos can traverse the matter without loss and some neutrinos interact close to the detector, so that the products of these neutrino interactions can be observed.

AMANDA data from the years 2000 to 2003 are analyzed to determine the energy spectrum of neutrinos, presenting for the first time the atmospheric neutrino spectrum in the energy range $2 - 200$ TeV. In Section 2, predictions for atmospheric neutrinos are reviewed. In Section 3, a conceptual overview of the issues involved in deconvolving a spectrum from observed data are discussed. In Section 4, more details of the data reduction, simulation and analysis method for the deconvolution of the neutrino spectrum are explained. Section 5 then describes a neural network used for the construction of an optimal energy-correlated variable, while Section 6 shows how the atmospheric spectrum is determined by regularised unfolding, and discusses the sources of statistical and systematic uncertainties that enter the calculation. Section 7 summarises the results while Section 8 discusses them in the context of other experimental results and flux predictions. Finally, Section 9 gives the conclusions from this analysis along with an outlook on the possibilities for IceCube, the successor of the AMANDA experiment.

2. Atmospheric neutrinos

When cosmic rays traverse the Earth's atmosphere, hadronic showers are produced by their interactions with the atmosphere. Depending on the energy of the primary cosmic ray, different secondaries can be produced. Up to energies of ~100 TeV, the flux is dominated by pion and kaon decays. This flux is usually referred to as the conventional atmospheric neutrino flux. The expected power-law spectrum of conventional atmospheric neutrinos is typically one power steeper than the primary cosmic ray spectrum: charged pions and kaons have rest-frame lifetimes of the order of 10^{-8} s. High-energy pions and kaons travel far enough in the atmosphere that they may interact with atmospheric nuclei before they decay. As the lifetime increases with the particles' energy, high-energy pions and kaons have a higher-probability to interact before decaying, which steepens the spectrum by one power. An analytic description of the neutrino spectrum between 100 GeV and $5.4 \cdot 10^5$ GeV is given by Volkova and Zatsepin [41]:

$$\frac{dN}{dE_\nu d\Omega}|_{\nu_\mu}(E_\nu,\theta) = A_\nu \cdot \left(\frac{E_\nu}{\mathrm{GeV}}\right)^{-\gamma} \cdot \left[\frac{1}{1+6E_\nu/E_\pi(\theta)} + \frac{0.213}{1+1.44E_\nu/E_{K^\pm}(\theta)}\right], \quad (1)$$

with $A_\nu = 0.0285$ GeV^{-1} cm^{-2} s^{-1} sr^{-1} and $\gamma = 2.69$. Here, E_π and $E_{K^\pm}$ are energy distribution parameters that depend on the zenith angle θ [41]. Eq. (1) covers the energy range relevant for this analysis, and will be used to fit the observed spectrum.

The energy spectrum varies with the zenith angle, as a pion traveling through the atmosphere horizontally ($\cos(\theta) = 1$) experiences a smaller density gradient than a pion traversing the atmosphere vertically ($\cos(\theta) = 0$). Thus, nearly vertical pions have a higher-probability of interacting with the atmosphere, which reduces the flux compared to the horizontal component. Other predictions of conventional atmospheric neutrino fluxes are given by Gaisser [21], Barr [5] and Honda [31], Honda [32], with uncertainties in the modeling of around 15% [6].

The prompt atmospheric neutrino flux is a second component in the atmospheric neutrino spectrum and is due to the decay of charm and bottom hadrons, which contain charm quarks. Since D^- and $\Lambda_c^\pm$ hadrons have lifetimes shorter than 10^{-12} s, they decay before any further interaction with the ambient matter can take place. Thus, these hadrons produce an isotropic neutrino spectrum whose shape is close to the primary cosmic ray spectrum, i.e. $E^{-2.7}$.

The atmospheric neutrino energy spectrum has so far been measured in the range 1–10 TeV [15,25,1]. The flux is found to follow the prediction of the conventional atmospheric flux within uncertainties. Here, the atmospheric neutrino spectrum extending up to 200 TeV is presented for the first time. As theoretical uncertainties increase towards higher-energies, the experimental investigation of the atmospheric spectrum can lead to conclusions about particle interactions, possible charm contribution or a possible extraterrestrial component.

3. Determination of the neutrino energy spectrum

Determination of the neutrino energy spectrum in a detector like AMANDA is complicated by various factors. Neutrino energies are not measured directly but are inferred from measuring the energies of the interaction products of the neutrinos. The three flavors of neutrinos produce different secondary patterns of particles in a detector, with correspondingly different correlations to the primary energy. An electron–neutrino will deposit most of its energy into an electromagnetic or hadronic cascade, which, limited by the resolution of the energy reconstruction algorithm, will correlate directly to the primary energy. A tau-neutrino produces two cascades of particles, one from the initial interaction and a second from the decay of the tau particle. If the energy of the event is sufficiently small, then both of these may be contained in the detector and thus be representative of the neutrino energy. For the main signature in AMANDA, upward moving muon tracks, the neutrino energy cannot be directly measured, because of the range of the muon. For a neutrino that interacts inside the detector, the muon may carry away a significant fraction of the neutrino energy which is then not measured. For high-energy neutrinos that interact very far away, the energy deposited in the detector from the final muon will only correlate weakly with the neutrino energy. This further degrades the correlation to the initial energy. Moreover, whatever

[4] Here and throughout the paper, we use the same notation for particles and anti-particles.

energy algorithm is used, its limited resolution will further degrade the ability of the experiment to measure a particle spectrum.

In practise, one uses knowledge of the neutrino physics and detector response to infer the parameters of the primary neutrino spectrum. Mathematically, this inference is represented by an integral equation,

$$p(y) = \int A(y,E) \cdot \Phi(E) dE + b(y), \quad (2)$$

where $p(y)$ is the probability of observing an event with a reconstructed parameter vector y, $A(y,E)$ represents the detector response to initial particles of energy E, $\Phi(E)$ is the neutrino flux and $b(y)$ is the non-neutrino background. Here, $p(y)$ represents the distribution of some parameter related to the energy of the event, e.g. the total deposited energy, or a direct estimate of the particle energy. Once $p(y)$ is obtained and $A(y,E)$ is determined via detector calibration and simulation, then there are several ways to infer $\Phi(E)$. The simplest is to take theoretical estimates of $\Phi(E)$ and see which one results in an expected $p(y)$ that fits the data best. If the theory can be parameterised, then these parameters can be adjusted until a best fit is found and errors on the parameters can be determined. Examples of this would be direct fitting of the slope γ and normalisation C of a spectrum of the form $\Phi(E) \sim C \cdot E^{-\gamma}$.

Another method employed in AMANDA is to assume the general form of a theoretical flux from a calculation and fit for a free normalisation and deviation from the spectral shape. These methods are commonly known as *forward folding*-the parameters of the flux are adjusted and then forward propagated through to an observable which is compared with data. In principle, the flux can be made theory independent by choosing a parametric form with a large number of parameters. This leads to a problem where small statistical fluctuations in the observed data may result in unphysical solutions for the spectrum, manifesting as bumps and dips in the spectrum. Methods known as regularisation are employed, whereby constraints on the smoothness of the solution are imposed, to control these effects. For the low-parameter methods, regularisation is built into the solution, for instance by the assumption of a power-law spectral form.

As the number of parameters grows, the computational time to solve for the best fit set of parameters also increases. As an alternative, non-iterative methods, collectively known as *unfolding methods*, exist for the direct solution of the high-parameter problems. The difficulties of regularisation are still inherent in these direct methods, just as they are in the interative forward folding methods. These considerations aside, the conceptual basis of unfolding is to use the direct inverse of the matrix $A(y,E)$ to solve for $\Phi(E) = A(y,E)^{-1} p(y)$.

The accuracy of a deconvolution of the spectrum using any of the methods improves on finding an observable y (which is possibly vector-valued) that is well correlated to the neutrino energy, manifested by minimising the influence of the off-diagonal elements of the matrix $A(y,E)$. There is an irreducible component of the off-diagonal elements set by the physics of neutrino interaction and muon propagation. For instance, the fact that the muon carries away only a fraction of the neutrino energy and then loses energy as it propagates to the detector reduces the correlation of the muon energy to the original neutrino energy. The size of the off-diagonal elements depends on how well correlated the chosen variables are with the neutrino energy. In this work, the energies of the muons are reconstructed by using a neural network, making use of six energy sensitive variables. The output of the neural network, along with two other energy sensitive parameters, form the observable y for the unfolding.

We do not directly unfold the atmospheric neutrino spectrum but unfold an intermediate spectrum which is a convolution of the actual flux with the probability of the neutrinos having passed through the Earth and with the efficiency for detection. Thus, the initial unfolding returns a neutrino spectrum with the same number of events as observed in the detector. This is then corrected as a function of energy and angle back to the true atmospheric spectrum.

4. The data set and the analysis method

For the determination of the neutrino energy spectrum from 2–200 TeV, 807 days effective livetime of data taken by the AMANDA detector between the years 2000 and 2003 are used. The selection of neutrino candidates for zenith angles $\theta > 90^\circ$ is presented in Achterberg et al. [2]. In a final step, tracks with $\theta < 100^\circ$ are removed to minimise the atmospheric muon contamination of the neutrino sample. The final sample contains 2972 neutrinos [36] and includes a background of less than 1% misreconstructed atmospheric muons [2].

In order to avoid possible biases we perform a blind analysis in the following sense: The properties of the selected events are initially checked on 10% of the full data set, by comparing this reduced data set to simulations of the atmospheric muon background and the conventional atmospheric neutrino flux. The simulation is done by using the air shower simulation CORSIKA for the background [28] and the neutrino generator *nusim* for the atmospheric contribution [29], see Fig. 1. The neutrino generator takes into account the interaction of the neutrinos with the Antarctic ice. Then, the tracks of the neutrino-induced muons are simulated in the muon propagation Monte Carlo *mmc* [12]. Finally, the detector simulation AMASIM [34] is used to simulate the emitted Cherenkov light and to emulate the hardware behaviour.

The same event selection applied to the experimental data set are used on the simulated data to identify the energy sensitive variables for the analysis. The simulation data and the 10% experimental data set are compared to verify the consistency of the event selection. This is essentially the approach used in a previous AMANDA analysis of the same up-going neutrino data set to obtain limits to the extraterrestrial neutrino flux [2].

After having optimised the analysis on the 10% subset of the data, the full data set is used to determine the energy spectrum of the detected up-going neutrino-induced events. These events are expected to pile up at energies below 2 TeV. Given the high-estimated purity of the investigated data set in terms of neutrinos [2], its energy spectrum is expected to be consistent with an atmospheric spectrum. While the theoretical predictions of the shape of this spectrum only show minor deviations between 2 TeV and 20 TeV, at energies between 20 TeV and 200 TeV deviations due to the unknown contribution of prompt neutrinos in this case a slight flattening of the spectrum are possible. Neutrinos of extraterrestrial origin are expected to significantly flatten the spectrum at even higher-energies.

A schematic view of the analysis chain is shown in Fig. 1. Six energy dependent observables are used as input variables for a neural net in order to produce a combined, optimised energy variable (Section 5). The combined variable is taken together with one further observable plus one of the variables entering the neural net, the latter still containing a component orthogonal to the NN output. With the three partially independent variables, the neutrino energy spectrum can be determined using regularised unfolding (Section 6). The resulting spectrum contains the effective number of events. As consequence of the unfolding, the probability density function of each event is distributed to several bins of the energy spectrum leading to broken event numbers in the spectrum. By relating the simulated neutrino energy spectrum to the effective number of events obtained by unfolding the simulated flux, the energy spectrum of the effective number of events of the measured

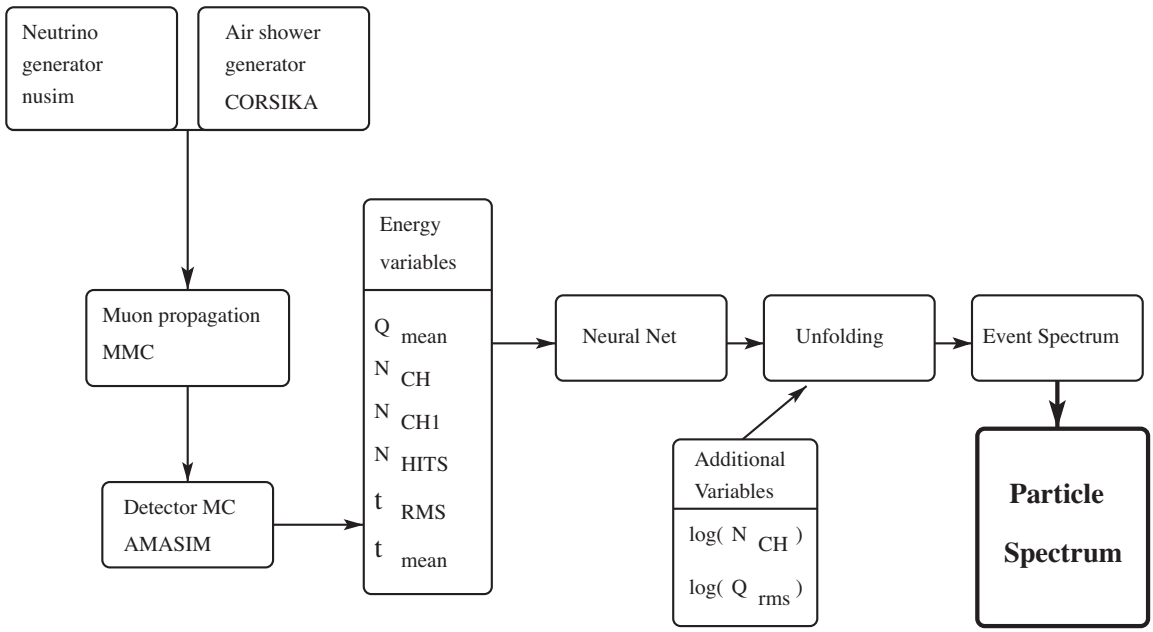

Fig. 1. Scheme of the simulation and analysis chain.

data is finally normalised to obtain the absolute neutrino energy spectrum.

5. Selection of energy dependent variables

Due to the limited acceptance and finite resolution of the detector, the reconstruction of the neutrino energy spectrum can be obtained only with unfolding methods. For this analysis, the method of regularised unfolding is used according to the RUN algorithm by Blobel [9, 10]. This algorithm allows up to three energy dependent variables as input for the unfolding procedure. Therefore, a set of three variables correlated to the neutrino energy is selected.

In a first step, the following seven observables[5] which show the best correlation with the generated neutrino energy in simulations, are selected from all variables well described by the simulation.

- N_{CH1}: The number of OMs (channels) having detected exactly one photon as signal during the event. Due to the stochastic energy losses of the muons, the number of emitted Cherenkov photons and hit OMs increases with the muon energy.
- N_{CH}: The number of OMs (channels) having detected one or more photons as signal, which increases with increasing muon energy.
- N_{HITS}: The total number of signal photo electrons within the event, which increases with increasing muon energy. Each OM can contribute to an event by the detection of one or more photoelectrons counted in this variable.
- t_{mean}: The average photon arrival time, i.e. the sum of all recorded photon arrival times relative to the trigger time, divided by the total number of hit optical modules. The higher the neutrino or muon energy, the more the mean time is shifted to late arrivals.
- t_{RMS}: The root mean square of the arrival time distribution of the photons, which grows with the number of late photons generated i.e. in secondary energy losses.
- Q_{mean}: The sum of all measured charges, in units of photoelectrons, divided by the number of hit OMs. This is equivalent to the mean number of recorded Cherenkov photons and is correlated to the energy.
- Q_{RMS}: The root mean square of the charge distribution of the photons in each OM, which grows with the maximal number of photons from secondary energy losses.

Some of these variables are correlated and their number exceeds the maximum of three allowed as input for RUN. As a consequence of a multitude of tests, in a second step, the first six variables are combined through a neural network (NN) to give one energy dependent variable. The NN output is then used together with log (N_{CH}) and log (Q_{RMS}) as the three inputs to the RUN algorithm.

The neural network is a standard back-propagation Multi-layer Perceptron (MLP) with two hidden layers used in a 6-6-3-1 feed-forward architecture (Fig. 2).

The complete simulation chain is used to generate a training set of muon events, with energies uniformly distributed in equidistant logarithmic energy bins between 500 GeV and 5 PeV and with trajectories uniformly distributed throughout a cylindrical volume with 400 m radius around the detector center. The NN is trained and tested with muon data sets, each containing 100,000 events.

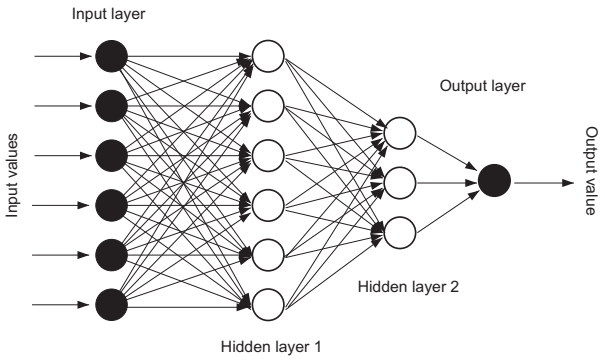

Fig. 2. Topology of the NN used for the data analysis.

[5] Six observables are used as first input and an additional one is used at a later stage of the analysis.

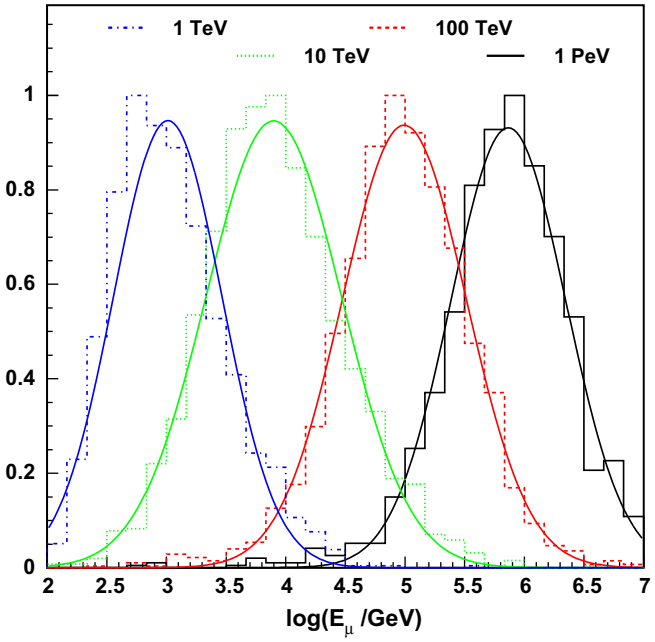

Fig. 3. Output of NN for the analysis of mono-energetic muons. The muons are simulated with fixed energies of 110,100 and 1000 TeV.

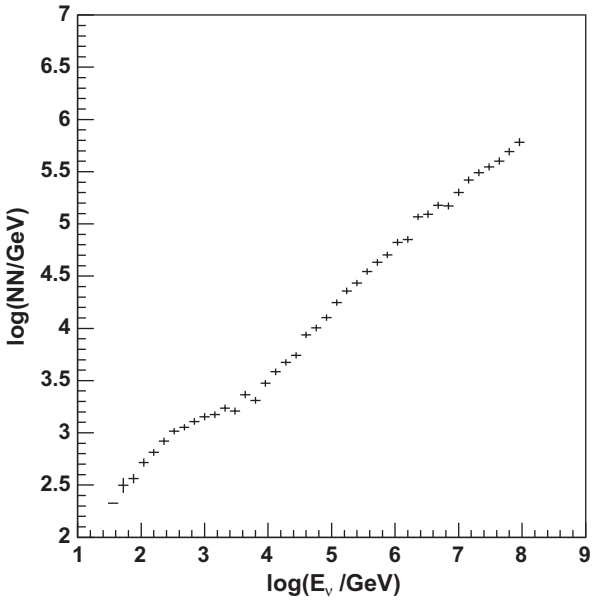

Fig. 4. Correlation between NN output and true neutrino energy. Here, the mean value of the NN output with its errors as a function of the true neutrino energy is shown. From the NN output, the neutrino energy can be determined with a standard deviation of about 0.5 order of magnitude.

Table 1
Resolution of the NN output. Here, E_μ is the true input energy, E_{mean} is the mean energy of the output and σ is the standard deviation from E_{mean}. All values are given in logarithmic units.

$\log_{10}(E_\mu/\text{GeV})$	$\log_{10}(E_{\text{mean}}/\text{GeV})$	$\log_{10}(\sigma/\text{GeV})$
3.0	3.03	0.42
4.0	3.92	0.58
5.0	4.99	0.51
6.0	5.86	0.48

The simulated events are then reconstructed and processed in the same way as the experimental data.

The energy resolution of the NN output is estimated with four test sets of mono-energetic muons, generated in the same way as the training set and with muon energies of 1 TeV, 10 TeV, 100 TeV, and 1 PeV. The resulting performance of the neural net and the corresponding resolutions are shown in Fig. 3. The neural net output can be fitted with a Gaussian distribution around the logarithm of the expected energy value. The results for the parameters of the fitted Gaussians are given in Table 1.

Fig. 4 shows how the NN output correlates to the neutrino energy, and justifies its use as input for the spectrum unfolding. The comparison of the NN output for simulated and experimental data (Fig. 5) shows good agreement. The agreement in slope depends on the neutrino energy spectrum chosen for the simulation. The apparently somewhat steeper decrease of the NN output predicted for a simulation according to Honda et al. [31] will be consistently visible also in the comparison of the final unfolding result (Fig. 9) with different flux predictions.

6. Determination of the energy spectrum

Following the notation introduced in Section 3, we form the energy sensitive variable y as the vector combination of the neutral network output, the logarithm of the number of channels fired and the logarithm of Q_{RMS}. The probability distribution of this vector variable is $p(y)$, leading to the need to solve for $\Phi(E)$ in the equation $p(y) = \int A(y,E) \cdot \Phi(E) dE + b(y)$.

By binning the generated energy distribution and the recorded parameter, this integral equation can be transformed to a linear matrix equation

$$\vec{y} = \mathbf{A} \cdot \vec{E} + \vec{b}. \tag{3}$$

The vectors $\vec{y}, \vec{E}$ and $\vec{b}$ represent the histograms containing the distribution of the observable, the sought-after energy spectrum and the distribution of the background. The kernel **A** contains the design matrix, describing the statistical detector properties. The off-diagonal terms in the kernel arise from the finite resolution of the energy estimators. Solving this equation by inversion leads to an ill posed problem because the transfer matrix **A** necessarily contains off-diagonal elements much smaller than unity, which in turn prevents the calculation of an *a priori* stable solution. To stabilise the solution, proper assumptions about the curvature of the solution have to be introduced to cut off insignificant elements of the matrix **A**.

In the RUN algorithm [9,10], the probability distributions used to unfold spectra on the basis of given observed parameters are parametrised in the form of a superposition of cubic *B*-splines of fourth order. The possible curvature of the solution is controlled by the number of degrees of freedom and the number of knots of the spline-superposition. If the number of degrees of freedom is too small it would damp significant amplitudes and smooth the solution too strongly; too many degrees of freedom could enforce unphysical wiggles in the solution. The number of knots of the spline is of only little influence on the result if chosen much higher than the number of degrees of freedom. This procedure is called regularisation and implemented in the unfolding algorithm RUN.

For the given experimental situation, the problem simplifies to the determination of an approximately linearly decreasing function if, instead of determining $\Phi(E)$ from y, $\log(\Phi(E))$ is calculated from $\log(y)$. To obtain an optimal parameter combination, extensive simulation tests of the following form were carried out: first, the transfer matrix **A** is calculated with an arbitrary[6] neutrino energy spectrum, a specific setting of the smoothing regularisation

[6] It is verified that there are no relevant effects for the unfolding results, if training spectra and true spectra do not deviate more than ±1 in the spectral index.

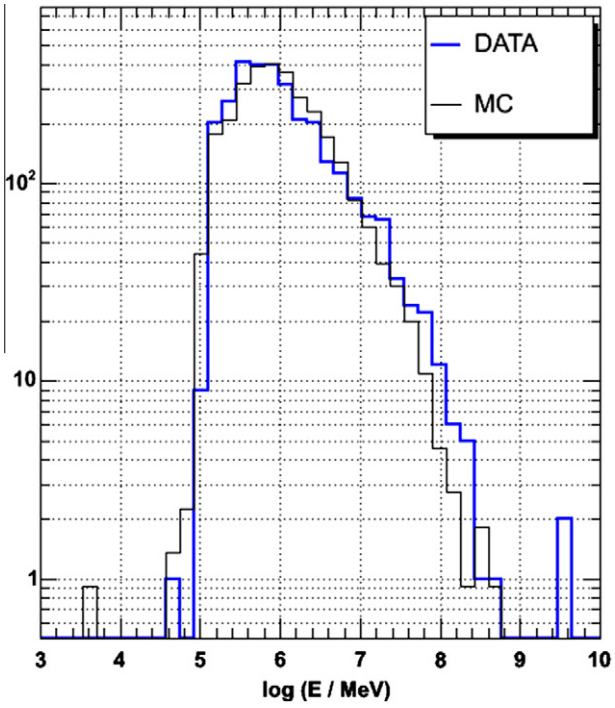

Fig. 5. Comparison of the neutrino energy NN output for data and a Monte Carlo simulation using the parametrisation of atmospheric neutrinos from [31].

parameter and a specific binning in $\vec{y}$ and $\vec{E}$. The used number of degrees of freedom is 5 and the number of knots 26 (see Blobel [9], Blobel [10] for a description of the structure). With this setting of the regularisation parameter, a possible flattening of the spectrum is visible in all tested cases. The unfolding result is restricted to be positive and the RUN internal histogram used to calculate the acceptance correction is smoothed.

Using these settings, different simulated spectra were unfolded. In total, the unfolding quality is checked with 278,000 Monte Carlo data sets. Each of them contains the unbiased statistical equivalent of one year of AMANDA data, a combination of atmospheric neutrinos and added signal contributions with an E^{-2} spectrum. For signal contributions proportional to E^{-2} ranging up to an contribution of 10^{-6} GeV cm^{-2} s^{-1} sr^{-1}, 1,000 independent unbiased Monte Carlo data sets, each containing one year of AMANDA data are produced. These Monte Carlo sets were checked to see if a flattening of the neutrino energy spectrum towards high-energies would be observed if such a signal were present. Also, the statistical errors obtained with the algorithm for the given binning follow a Gaussian (or for small effective number of events, a Poissonian) distribution. The chosen unfolding parameters would smooth out spikes on top of the spectrum smaller than the bin width in the middle and lower side of the investigated energy range.

An essential part of the unfolding procedure is the proper estimation and accounting of the uncertainties, statistical and systematic, that propagate through the unfolding to determine the error bars on the spectrum. In RUN the statistical error is calculated under the assumption that Poissonian and Gaussian statistics can be applied. The same analysis shows that the distribution of the unfolding results for every bin follows a Gaussian. It further shows that towards high-energies a flattening of the spectrum is visible with the chosen method if an extra signal component is present.

In addition to the statistical errors, there are several sources of systematic uncertainty that affect the estimation of the unfolding matrix and thus propagate through the unfolding to the error bars on the physical atmospheric neutrino spectrum. Estimates of the uncertainties due to the response of the detector are quantified in Achterberg et al. [3]. Here, we discuss additional sources of uncertainty from the neutrino cross sections and muon propagation, which both influence the rate and angular distribution of the detected events.

The neutrino–nucleon DIS cross section has been measured directly at accelerators up to only ~350 GeV [4]. At much higher-energies, deep inelastic scattering probes a kinematic region (high Q^2 and low Bjorken x) where the parton distribution functions have not been directly measured. The CC ν N cross sections used for this paper are calculated as in [22,37], with details given in [23]. The calculations use the QCD inspired dynamical small x predictions for parton distributions according to the radiative parton model [24] and lead to the conclusion that the systematic uncertainty in the investigated energy range is well below 10%. Also, a recent exercise carried out at next-to-leading order using the ZEUS global PDF fits has provided the neutrino cross section from 10^3 GeV up to 10^{12} GeV with an estimated uncertainty ranging between ±3% and ±14% [13].

The systematic errors due to muon energy loss, ice properties and effective efficiency of the photomultipliers can be estimated by comparing the reconstructed and expected slope of the depth intensity relation of atmospheric muons.

This deviation depends on a number of factors relevant for light detection, including the muon energy loss, Cherenkov light propagation effects and the effective efficiency of the Cherenkov light detection.

The average range of a muon is approximately $R = 1/b \ln(1 + b/a \cdot E)$, where a and b are the effective energy loss parameters for ionisation and the sum of the stochastic processes (bremsstrahlung, pair production and photonuclear interactions) respectively. They are related to the energy loss rate through $dE/dx = a + b \cdot E$.

Although the total cross section can be calculated with high-precision, the spectral averaged energy parameter b, in the sense used here closely connected to the Cherenkov light produced by the stochastic energy losses, can only be estimated to a precision of a few percent.

The probability of detecting emitted Cherenkov light depends on both on light propagation through the ice and the effective efficiency ϵ of the optical modules.

Comparing the slopes of depth intensity relation of atmospheric muons in Monte Carlo and data allows us to set an upper limit on the averaged systematic uncertainties. In addition to the factors relevant for the muon detection, this deviation also contains effects due to the model dependent muon production in the atmosphere. For this analysis, the maximal deviation in slope was 10%.

This uncertainty in slope transfers directly to the neutrino flux calculation. Combining all the independent detector systematics from Achterberg et al. [3] of (8%) with the cross section (10%) and the muon propagation uncertainties (10%) gives a total uncertainty in flux of 16% which is applied to the statistical error bars from the unfolding.

7. Energy spectrum of atmospheric neutrinos between 2 TeV and 200 TeV

In a first step, an intermediate energy spectrum, is determined from the data and compared to simulation results in Fig. 6. This result physically corresponds to the convolution of the true physical atmospheric neutrino spectrum and the neutrino survival and detection efficiency, i.e. effective area of the detector [2]. The final neutrino spectrum will later be found by correcting for the effective area and observation time. The energy distribution of the

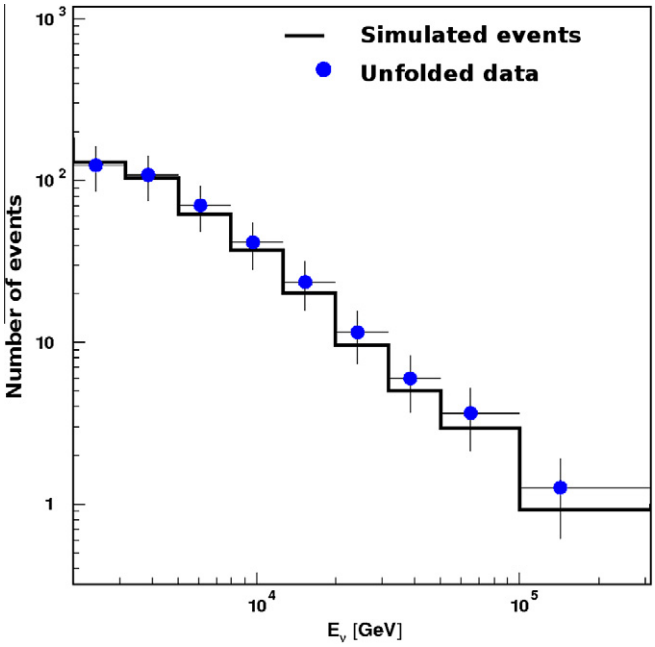

Fig. 6. Comparison of the energy distribution of the effective number of events obtained by unfolding the data of the years 2000–2003 (data points) and an event distribution simulated according to Volkova and Zatsepin [41] (histogram).

Table 2
Effective number of events obtained by the unfolding of the neutrino data of the years 2000 to 2003.

log (E_ν/GeV)	Number of events
3.3–3.5	124
3.5–3.7	108
3.7–3.9	70.3
3.9–4.1	41.6
4.1–4.3	23.6
4.3–4.5	11.5
4.5–4.7	5.96
4.7–5.0	3.64
5.0–5.5	1.26
5.5–6.0	0.00

Table 3
Results of the Gaussian fit to simulated data. In the first two columns the energy bins are given, A_ν is the normalisation, E_r the reconstructed mean energy and σ the width of the distribution.

log (E_ν/GeV)	A	log (E_r/GeV)	σ
3.5–3.7	0.15	3.56	0.48
3.7–3.9	0.16	3.76	0.46
3.9–4.1	0.15	4.01	0.43
4.1–4.3	0.17	4.22	0.41
4.3–4.5	0.18	4.41	0.43
4.5–4.7	0.20	4.61	0.46
4.7–5.0	0.30	4.92	0.50
5.0–5.5	0.44	5.39	0.49
5.5–6.0	0.38	5.73	0.44

effective number of events[7] obtained by unfolding the data of the years 2000–2003 and a distribution of events simulated according to Volkova and Zatsepin [41] are compared. Shown is the number of events averaged in the investigated zenith angular range from 100° to 180°. The error bars include the systematic errors of 16%. For $E > 2$ TeV, the unfolded spectrum agrees with this prediction within the errors. The corresponding number of events for the unfolded spectrum are given in Table 2.

In order to understand and demonstrate the effects of the energy resolution, a further check is performed. The events in the final simulated data set are split up into nine different energy sets based on the known true energy of the primary neutrino. Each of these event sets are then independently unfolded using the same algorithm as for the full data set. The widths of the resulting individual spectra give an indication of the energy resolution of the experiment. Each spectrum is fitted to a Gaussian

$$F(\log(E_\nu/\mathrm{GeV})) = A \cdot \exp\left\{-\frac{1}{2}\left(\frac{\log(E_\nu/\mathrm{GeV}) - \log(E_r)}{\sigma}\right)^2\right\}. \quad (4)$$

The results of these fits are given in Table 3. The width of the energy bins denote the energy range to which the unfolding and the corresponding errors refer. Since the energy resolution obtained with the method described is between 0.4 and 0.5 in log (E_ν) (see Table 3), the contents of the bins in the final spectrum are correlated. The statistical errors obtained by regularised unfolding account for this fact. With the discussed method, within the investigated energy range a mean energy resolution of 0.45 in log (E_ν/GeV) is reached.

In the final step, to obtain the actual energy spectrum of the primary atmospheric neutrinos, the "at the detector" neutrino spectrum is corrected for the detector efficiency and neutrino survival probability. This physical energy spectrum of atmospheric muon and anti-muon neutrinos is presented in Fig. 7.

Table 4 lists the values for the measured neutrino spectrum $dN_\nu/dE_\nu \cdot E_\nu^2$ for each energy bin. In the highest-energy bin, the error bars are compatible with a flux equal to zero. A fit according to Eq. (1), with the normalisation of the spectrum A and the spectral index γ as free parameters yields

$$A_\nu = (0.022 \pm 0.026)\ \mathrm{GeV}^{-1}\ \mathrm{cm}^{-2}\ \mathrm{s}^{-1}\ \mathrm{sr}^{-1}, \quad (5)$$
$$\gamma = 2.55 \pm 0.13. \quad (6)$$

These values are compatible with the theoretical prediction by Volkova and Zatsepin [41], $A|_{\mathrm{Volkova}} = 0.0285\ \mathrm{GeV}^{-1}\ \mathrm{cm}^{-2}\ \mathrm{s}^{-1}\ \mathrm{sr}^{-1}$ and $\gamma|_{\mathrm{Volkova}} = 2.69$. The error of A_ν is compatible with zero, since it represents the flux at 1 GeV, while measurements are performed at above 100 GeV.

8. Discussion of the atmospheric energy spectrum

Fig. 8 compares the unfolded energy spectrum (blue dots) to previously measured energy spectra. Measurements by the Fréjus experiment are shown as red squares [15]. The red lines represent SuperK measurements [25]. The latter result is given in the form of a band of possible values indicated in this plot as an upper and a lower line. Allowed values (90% confidence level) lie between those two lines. The blue lines at higher-energies represent AMANDA measurements, based on the same data sample, but optimised for low-energies [1]. Again, results are presented in form of a band, lying between the upper and lower line. All measurements are for the sum of neutrinos and anti-neutrinos. Although the low-energy AMANDA analysis is based on the same data set as this analysis, it is fundamentally different from the high-energy analysis based on an extended regularised unfolding algorithm discussed here. The low-energy analysis presented in [1] used the concept of forward folding. A set of curves with a limited number of parameters is used to give an estimate of the input energy spectrum. In this spe-

[7] As discussed in Section 6, single recorded events contribute in general to several energy bins of the unfolded energy spectrum. The summed weights are called effective event numbers.

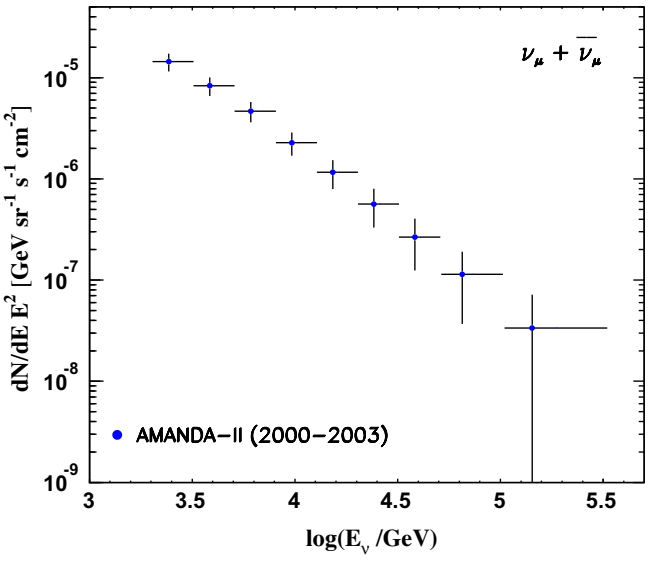

Fig. 7. The unfolded energy spectrum of muon-and anti-muon neutrinos in the atmosphere, measured with AMANDA.

Table 4
The unfolded energy spectrum of muon and anti-muon neutrinos in the atmosphere, using AMANDA data from the years 2000–2003. The errors give the 68% C.L. interval on the unfolded flux.

$\log(E_\nu/\text{GeV})$	$dN/dE_\nu \cdot E_\nu^2 [10^{-7}$ GeV/s/sr/cm$^2]$
3.3–3.5	140^{+26}_{-27}
3.5–3.7	83^{+15}_{-16}
3.7–3.9	47^{+9}_{-10}
3.9–4.1	23^{+5}_{-6}
4.1–4.3	12^{+3}_{-3}
4.3–4.5	$5.6^{+1.9}_{-2.4}$
4.5–4.7	$2.7^{+1.0}_{-1.4}$
4.7–5.0	$1.1^{+0.5}_{-0.5}$
5.0–5.5	$0.34^{+0.20}_{-0.34}$

cial case, the prediction by Gaisser et al. [21], Barr et al. [5], Barr et al. [7] is used with varying normalisation and spectral index to determine the spectrum. This method is most sensitive to the median energy of the sample, which is around 640 GeV and is therefore not optimal for investigations at high-energies.

These results are the first measurement of the atmospheric neutrino spectrum at energies up to 200 TeV. Limits to an extraterrestrial neutrino flux with a generic E^{-2} spectrum are shown as dashed lines in Fig. 8. The Fréjus limit is shown at energies between $10^{3.2}$ GeV and 10^4 GeV. A limit derived from the same AMANDA data set used here was presented in Achterberg et al. [2], confirming that no significant contribution from extraterrestrial sources at energies between $10^{4.2}$ GeV and $10^{6.4}$ GeV can be identified at the current sensitivity level.

The unfolded neutrino energy spectrum is compared to different predictions of the conventional neutrino flux in Fig. 9. As the measured neutrino spectrum includes zenith angles in the range $100° < \theta < 180°$, the predictions are angle-averaged for comparison and the sum of muon and anti-muon neutrinos is used. The conventional atmospheric neutrino flux depends on parameters which lead to uncertainties in the prediction of the expected flux [6]. We compare the measured result with different predictions for this flux. The analytic approximation by Volkova and Zatsepin [41] is shown as the dot-dashed line. The solid line represents the Bartol prediction [21,5,7]. The flux calculcated by Honda et al. [32] is

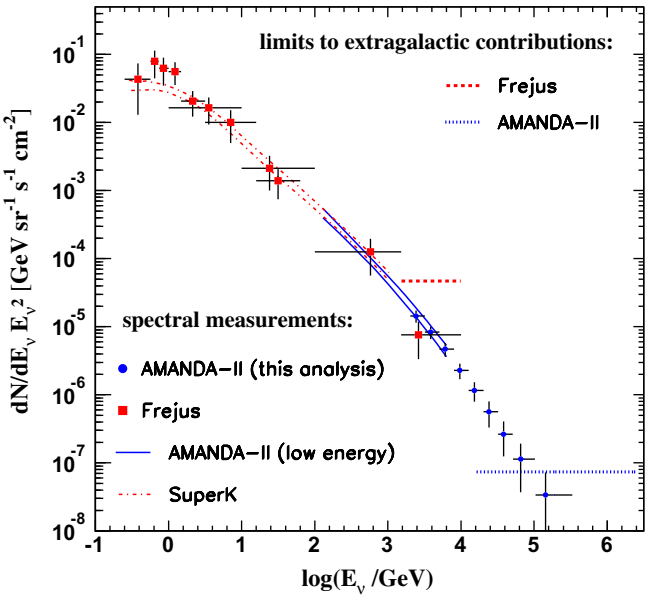

Fig. 8. The unfolded spectrum from this analysis (blue dots) compared to other measurements of the atmospheric neutrino spectrum: Fréjus measurements (red squares) are from [15]. SuperK results (red lines) are presented in [25]. A measurement by AMANDA at low-energies (blue lines) is shown in [1]. Limits (dashed lines) are from Fréjus between $10^{3.2} - 10^4$ GeV [38] and from a high-energy analysis with AMANDA using the same data set as this analysis [2]. (For interpretation of the references to colour in this figure legend, the reader is referred to the web version of this article.)

shown as the dashed line. The measured spectrum is in good agreement with all three predictions for conventional neutrinos.

In Fig. 10, the measured energy spectrum is compared to the prediction of the combined spectrum of conventional and prompt neutrinos. For the conventional spectrum, the prediction made by Honda et al. [31] is chosen. For the prompt contribution, several different models are shown. The Recombination Quark Parton Models (*RQPM*) is phenomenology-based and non-perturbative, as described by Fiorentini et al. [20]. The shown *QGSM* model is half-empiric, i.e. a combination of theoretical modeling and accelerator data. This model uses the Quark Gluon String Model based on non-perturbative QCD calculations, presented by Costa [14]

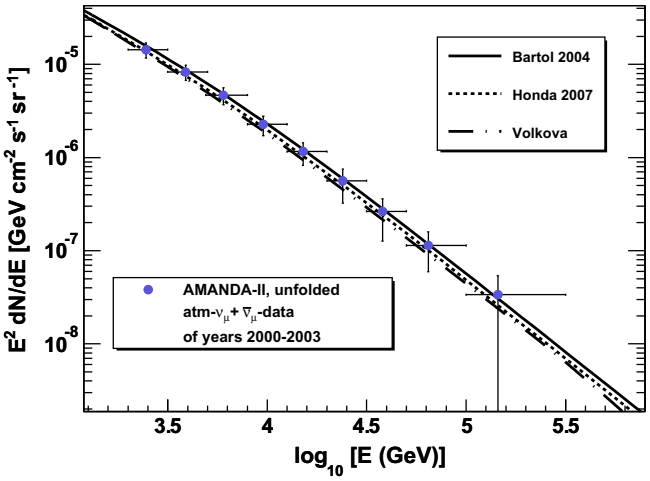

Fig. 9. Comparison of the unfolded energy spectrum to different predictions of the atmospheric neutrino flux, resulting from pion and kaon decays. The predictions are compatible with the measured spectrum within the given errors: [41] (dot-dashed line), [21,5,7] (solid line) and [32] (dashed).

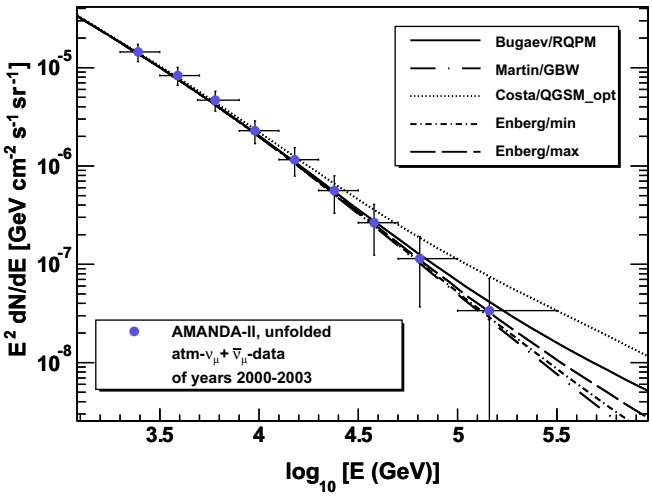

Fig. 10. The measured neutrino energy spectrum compared to predictions of a combination of conventional neutrinos [32] and prompt neutrinos. The different prompt models are: Fiorentini et al. [20], Bugaev et al. [11] (*Bugaev RQPM*, solid line); Martin et al. [35] (*Martin GBW*, dot-long-dashed line); Costa [14] (*QGSM-opt*, dotted line) and Enberg et al. [17] (*Enberg/min, Enberg/max*, dot-short-dashed and dashed lines).

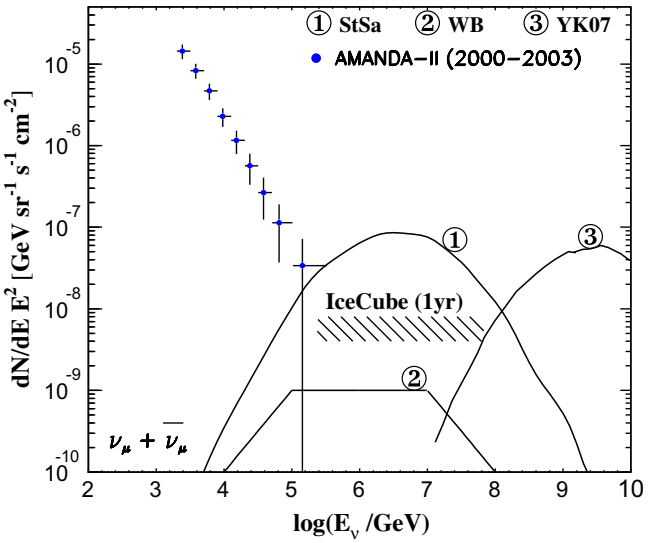

Fig. 11. Measured muon and anti-muon neutrino spectrum and predictions of extraterrestrial neutrino fluxes. Neutrinos are expected from e.g. Active Galactic Nuclei (e.g. Stecker and Salamon [40], Stecker [39], (1)), Gamma Ray Bursts (e.g. Waxman and Bahcall [42], Waxman and Bahcall [43], (2)) as well as from the interactions of ultra high-energy cosmic rays with the cosmic microwave background (e.g. Yüksel and Kistler [44], (3)). The expected sensitivity of IceCube to an E_ν^{-2} neutrino spectrum is in the range of the hatched area [33,26].

and Bugaev et al. [11], shown is the maximum prediction. Further predictions are given by Martin et al. [35]. A model by Enberg et al. [17] is shown in its minimum and maximum configuration. Uncertainties increase towards higher-energies as elaborated in Section 2. The highest-prediction (*QGSM opt*, Costa [14]) is still compatible with the error bars of the spectrum presented here. Next-generation experiments like IceCube will have a higher-sensitivity to a prompt component.

9. Conclusions and outlook

The unfolded muon and anti-muon neutrino energy spectrum is presented for the energy range 2 TeV and 200 TeV, constituting the first measurement at such high-energies. The spectrum is compatible with predictions of the conventional and prompt atmospheric neutrino spectra. The AMANDA detector was switched off in May 2009 but its more than 60 times larger successor IceCube is currently being built at the same South Pole location. As of February 2010, 79 strings have been deployed and completion is planned within a year, completing an instrumented volume of 1 km^3.

Fig. 11 shows the results of this analysis together with predictions for extraterrestrial neutrino fluxes. Typical neutrino fluxes from e.g. Active Galactic Nuclei or Gamma Ray Bursts are expected to follow a spectrum close to E_ν^{-2}, which is much harder than both the conventional ($\sim E_\nu^{-3.7}$) and the prompt ($\sim E_\nu^{-2.7}$) neutrino flux [27,8, e.g.]. This implies a flattening of the spectrum towards high-energies which is much more distinct than for prompt neutrinos. IceCube has the potential to observe this flattening of the spectrum, as its main sensitivity lies in the range $10^5 - 10^8$ GeV [33,26] and will be able to measure the high-energy neutrino spectrum with higher-accuracy and towards higher-energies than AMANDA within the first few years of operation.

Acknowledgements

We acknowledge the support from the following agencies: US National Science Foundation-Office of Polar Program, US National Science Foundation-Physics Division, University of Wisconsin Alumni Research Foundation, US Department of Energy, and National Energy Research Scientific Computing Center, the Louisiana Optical Network Initiative (LONI) grid computing resources; Swedish Research Council, Swedish Polar Research Secretariat, Swedish National Infrastructure for Computing (SNIC), and Knut and Alice Wallenberg Foundation, Sweden; German Ministry for Education and Research (BMBF), Deutsche Forschungsgemeinschaft (DFG), Research Department of Plasmas with Complex Interactions (Bochum), Germany; Fund for Scientific Research (FNRS-FWO), FWO Odysseus programme, Flanders Institute to encourage scientific and technological research in industry (IWT), Belgian Federal Science Policy Office (Belspo); Marsden Fund, New Zealand; Japan Society for Promotion of Science (JSPS); the Swiss National Science Foundation (SNSF), Switzerland; A. Kappes and A. Groß acknowledge support by the EU Marie Curie OIF Program; J. P. Rodrigues acknowledges support by the Capes Foundation, Ministry of Education of Brazil.

References

[1] R. Abbasi et al., IceCube Coll., Phys. Rev. D 79 (10) (2009) 102005.
[2] A. Achterberg et al., IceCube Coll., Phys. Rev. D 76 (4) (2007) 042008.
[3] A. Achterberg et al., IceCube Coll., Phys. Rev. D 75 (10) (2007) 102001.
[4] C. Amsler et al., Particle data group, Phys. Lett. B. 667 (2008) 1.
[5] G.D. Barr et al., Phys. Rev. D 70 (2) (2004) 023006.
[6] G.D. Barr, et al., 2006. arXiv:astro-ph/0611266.
[7] G.D. Barr, et al., 2009. <http://www-pnp.physics.ox.ac.uk/~barr/fluxfiles/>.
[8] J.K. Becker, Phys. Rep. 458 (2008) 173.
[9] V. Blobel, Unfolding methods in high-energy physics experiments, in: Proceedings of the 1984 CERN School of Computing. No. CERN 85-09. CERN , European Organization for Nuclear Research, Geneva, 1985, p. 88.
[10] V. Blobel, The RUN Manual-Regularized Unfolding for High-Energy Physics Experiments, Technical Note TN 361, OPAL, 1996.
[11] E.V. Bugaev et al., Nuovo Cim. C Geophys. Space Phys. C 12 (1989) 41.
[12] D. Chirkin, W. Rhode, 2004. arXiv:hep-ph/0407075.
[13] A. Cooper-Sarkar, S. Sarkar, J. High Energy Phys. 1 (2008) 75.
[14] C.G.S. Costa, Astropart. Phys. 16 (2001) 193.
[15] K. Daum et al., Zeitschrift für Physik C 66 (1995) 417.
[16] T. DeYoung et al., IceCube Coll., J. Phys. Conf. Ser. 136 (2) (2008) 022046.
[17] R. Enberg, M.H. Reno, I. Sarcevic, Phys. Rev. D 78 (4) (2008) 043005.
[18] E. Fermi, Phys. Rev. 75 (8) (1949) 1169.
[19] E. Fermi, Astroph. J. 119 (1954) 1.
[20] G. Fiorentini, V.A. Naumov, F.L. Villante, Phys. Lett. B 510 (2001) 173.
[21] T.K. Gaisser, et al., in: Proceedings of International Cosmic Ray Conference, vol. 5, 2001, p. 1643.
[22] K. Giesel, J. Jureit, E. Reya, Astropart. Phys. 20 (2003) 335.
[23] M. Glück, S. Kretzer, E. Reya, Astropart. Phys. 11 (1999) 327.
[24] M. Glück, E. Reya, A. Vogt, Eur. Phys. J. C 5 (1998) 461.

[25] C. Gonzalez-Garcia, M. Maltoni, J. Rojo, J. High Energy Phys. 10 (2006) 75.
[26] F. Halzen, 2008. arXiv:0809.1874.
[27] F. Halzen, D. Hooper, Rep Progress Phys 65 (2002) 1025.
[28] D. Heck, 1998. CORSIKA: A Monte Carlo Code to Simulate Extensive Air Showers, Forschungszentrum Karlsruhe Report RZKA 6019. URL <http://www-ik.fzk.de/corsika/physics_description/corsika_phys.html>.
[29] G. Hill, Ph.D. Thesis, University of Adelaide, 1996.
[30] M. Honda et al., Phys. Rev. D 52 (1995) 4985.
[31] M. Honda, Phys. Rev. D 70 (4) (2004) 043008. <http://link.aps.org/abstract/PRD/v70/e043008>.
[32] M. Honda et al., Phys. Rev. D 75 (4) (2007) 043006.
[33] K. Hoshina, J. Hodges, G. C. Hill, in: Proceedings of International Cosmic Ray Conference, vol. 5, 2008, p. 1449.
[34] S. Hundertmark, In: Proceedings of Simulation and Analysis Methods for Large Neutrino Telescopes. DESY Zeuthen, Germany, July 1999, p. 276, DESY-PROC-1999-01.
[35] A.D. Martin, M.G. Ryskin, A.M. Stasto, Acta Phys. Pol. B 34 (2003) 3273.
[36] K. Münich, Ph.D. Thesis, Universität Dortmund, 2007.
[37] E. Reya, J. Rödiger, Phys. Rev. D 72 (5) (2005) 053004.
[38] W. Rhode et al., Fr'ejus Coll., Astropart. Phys. 4 (1996) 217.
[39] F.W. Stecker, Phys. Rev. D 72 (10) (2005) 107301.
[40] F.W. Stecker, M.H. Salamon, Space Sci. Rev. 75 (1996) 341.
[41] L.V. Volkova, G.T. Zatsepin, Sov. J. Nucl. Phys. 37 (1980) 212.
[42] E. Waxman, J.N. Bahcall, Phys. Rev. Lett. 78 (1997) 2292.
[43] E. Waxman, J.N. Bahcall, Phys. Rev. D 59 (1999) 23002.
[44] H. Yüksel, M.D. Kistler, Phys. Rev. D 75 (8) (2007) 083004.